高等学校化学学报
CHEMICAL JOURNAL OF CHINESE UNIVERSITIES
研究论文

基于菲并[9,10]咪唑衍生物的 CIE_y<0.04的深蓝光热激子材料

葛书源#，冯梓浚#，程　壮，刘福通，路　萍
（吉林大学超分子结构与材料全国重点实验室，长春130012）

摘要　满足国际电信联盟(ITU)BT.2020标准的高性能深蓝光材料及发光器件目前仍然非常有限. 本工作将甲基取代的联苯基团接到经典的热激子基团——菲并咪唑上，设计并合成了4种深蓝光发光材料：PP1M、PP2M、PP3M和PP4M. 甲基的引入增大了分子的扭转角，从而拓宽了4种化合物的能隙. 通过对不同取代位点的调控，PP3M在非掺薄膜中实现了85.3%的荧光量子产率. 基于PP3M的掺杂器件表现出深蓝光发射，其外量子效率为7.2%，且具有较小的效率滚降. 该器件的半峰宽仅为53 nm，CIE坐标为(0.16，0.04)，符合BT.2020标准的要求. 研究结果显示，器件中高的激子利用率主要源于热激子机制. 本研究为开发兼具高发光效率与优异色纯度的高性能深蓝光OLED材料提供了可行的分子设计思路.

关键词　有机发光二极管；深蓝光；杂化局域-电荷转移激发态；外量子效率；菲并[9,10]咪唑
中图分类号　O626；O644.1　　**文献标志码**　A　　doi：10.7503/cjcu20250403

Deep-blue Hot Exciton Material Based on Phenanthro[9,10]imidazole Derivative with CIE_y<0.04

GE Shuyuan#, FENG Zijun#, CHENG Zhuang, LIU Futong, LU Ping*
(*State Key Laboratory of Supramolecular Structure and Materials*, *Jilin University*, *Changchun* 130012, *China*)

Abstract　High-performance deep-blue emitters that meet the BT. 2020 standard proposed by the International Telecommunication Union (ITU) for organic light-emitting diodes (OLEDs) remain highly limited. In this work, four deep-blue emitters, PP1M, PP2M, PP3M, and PP4M, are designed and synthesized by connecting methyl-substituted biphenyl groups with classical hot exciton building block of phenanthreneimidazole. The introduction of methyl groups contributes to increase the molecular torsion angle and widen the energy gaps for the four compounds. Through appropriate modulation of substitution site, PP3M achieves the highest photoluminescence quantum yield of 85.3% in neat film. As a result, the PP3M-based device exhibits deep-blue light with external quantum efficiency of 7.2% and suppressed efficiency roll-off. The device also shows a small full width at half maximum of 53 nm and the CIE coordinates locate at (0.16, 0.04), meeting well with the BT. 2020 standard. The high exciton utilization efficiency is primarily ascribed to the hot exciton pathway. This study provides a reliable insight for the design of efficient deep-blue OLEDs with high color purity.

Keywords　Organic light-emitting diode; Deep-blue light; Hybridized local and charge transfer state; External quantum efficiency; Phenanthro[9,10]imidazole

收稿日期：2025-12-29. 网络首发日期：2026-01-21.
联系人简介：路　萍，女，博士，教授，主要从事有机光电功能材料与器件性能方面的研究. E-mail：lup@jlu.edu.cn
基金项目：国家自然科学基金(批准号：22375072)资助.
Supported by the National Natural Science Foundation of China(No.22375072).
共同第一作者.

1 Introduction

Organic light-emitting diodes (OLEDs) which are considered as the promising technology for the next-generation full-color displays and solid-state lightings have attracted extensive attention in the past decades[1—5]. The deep-blue emitter is of significant importance in reducing the power consumption and broadening the color gamut in OLEDs. The traditional Commission International de L'Eclairage (CIE) coordinates criterion for deep-blue emission in OLEDs is (0.14, 0.08) as defined by the National Television System Committee (NTSC), and (0.15, 0.06) by the European Broadcasting Union (EBU)[6—8]. However, the increasing demand for next-generation high resolution displays, such as ultra-high definition TVs and smart phones, has further improved the requirement for the deep-blue emission with even higher color purity and wider color gamut[9—12]. The BT. 2020 standard of (0.131, 0.046) promulgated by the International Telecommunication Union (ITU) in 2012 has largely expands the chromaticity coordinates of primary colors which establishes a wide gamut color space covering ~75% of the visible spectrum in the CIE 1931 chromaticity diagram[13—15]. Accordingly, a more stringent requirement needs to be fulfilled for deep-blue material. Besides enhancing the color purity of deep-blue materials, improving electroluminescent efficiency is another crucial issue since the performance of deep-blue OLEDs is relatively backward compared with red and green ones[16—18]. According to limitation of spin-statistics, merely 25% of singlet excitons can be used in conventional fluorescent OLEDs[19,20]. In order to achieve electrically generated excitons as fully as possible, the thermally activated delayed fluorescence (TADF) and hot exciton materials have emerged after years of endeavors which can utilize the triplet excitons in the form of radiative transitions[21,22]. TADF materials have made rapid progress in the past years owing to their theoretically high exciton utilization efficiency (EUE) of 100%[23—25]. However, the first singlet excited state (S_1) in conventional TADF system typically exhibits strong charge transfer (CT) character, leading to relatively broad emission spectra[26,27]. Inspired by the work of Hatakeyama *et al.*, multiple resonance TADF (MR-TADF) materials with rigid structures have gained breakthroughs in narrowing emission spectra[28—31]. Yet, MR-TADF material meeting the BT.2020 standard remains particularly rare. In addition, the reported synthesis method of MR molecules is also complicated by introducing boron atoms with alkyl lithium, which often leads to the relatively low reaction yield and the difficulty in purifying the final product. Moreover, low-concentration doped devices is commonly needed to improve color purity and efficiency in OLEDs due to the planar rigid structure of MR molecules. These features severely hinder the commercialization of MR-TADF OLEDs. Since the pioneering work by Ma *et al.*[32], a number of high-efficiency emitters with hybridized local and charge-transfer (HLCT) excited state feature based on the hot exciton mechanism have been developed recently[32,33]. The hot exciton materials can achieve theoretical 100% EUE through the prompt high-lying reverse intersystem crossing (hRISC) from high-lying triplet states (T_n, $n\geqslant 2$) to singlet states (S_m, $m\geqslant 1$)[31]. Moreover, the S_1 state in such systems can be HLCT state or even local excited (LE) state with weak CT characteristic, rendering hot exciton emitters to be promising candidates to achieve high efficiency and good color purity simultaneously in deep-blue region[34—38].

In this work, a series of deep-blue emitters, PP1M, PP2M, PP3M, and PP4M, are designed and synthesized by modifying the classical phenanthro[9,10]imidazole (PPI) chromophore with methyl-substituted biphenyl units at various substitution sites. In PP1M and PP3M, the methyl groups are located on the benzene rings in the biphenyl segment to restrict the π-conjugation extension of the whole molecule. In contrast, PP2M and PP4M bear methyl substitutions on the benzene ring attaching to PPI, which can increase the torsion angles between the biphenyl and PPI units. In addition, the increasement in the number of methyl groups may

contribute to suppress the conjugation degree and raise the band gap (E_g) of resulting deep-blue emitters. As expected, both theoretical calculations and experimental results indicate that they all exhibit HLCT characteristics and the E_g values follow the order of PP4M>PP2M>PP3M>PP1M. Owning to the high oscillator strengths (f>1.50), PP1M and PP3M achieve high photoluminescence quantum yields (PLQYs) exceeding 70% in solid state. The PP3M-based doped OLED realizes the deep-blue emission peaking at 420 nm with a narrow full width at half maximum (FWHM) of 53 nm, and a small CIE_y value of 0.04, meeting well with the stringent BT.2020 standard. Furthermore, the device demonstrates a high external quantum efficiency (EQE) of 7.2% and a maximum luminance of 6030 cd/m^2 with small efficiency roll-off. This study provided a reliable molecular design strategy for high-performance deep-blue OLEDs.

2 Experimental

2.1 Materials and Instruments

Potassium carbonate (K_2CO_3, AR), tetrakis(triphenylphosphine)palladium[$Pd(PPh_3)_4$, AR, Pd≥9%], dichloromethane (DCM, AR), ethyl acetate (EA, AR), petroleum ether (PE, AR), and tetrahydrofuran (THF, AR) were purchased from Aladdin Reagent(Shanghai) Co., Ltd. and used as received.

Bruker ARX500 NMR spectrometer(500 MHz, using CD_2Cl_2 as solvent and tetramethylsilane as internal standard), Bruker, Germany; Scientific ITQ 1100 TMGC/MS^n mass spectrometer (MS), Thermo Fisher Scientific, USA; RF-5301 PC fluorescence spectrophotometer, Shimadzu, Japan; LS 45 spectrophotometer PerkinElmer, USA; 100W electrochemical workstation (with platinum working electrode, Ag/Ag$^+$ reference electrode, and platinum wire counter electrode), BAS, USA; Q500 Thermogravimetric analyzer (TGA) (under N_2 atmosphere), TA Instruments, USA; DSC-204 Differential scanning calorimeter (DSC) (under N_2 atmosphere), Netzsch, Germany.

2.2 Synthesis and Characterization

PP1M, PP2M, PP3M and PP4M were prepared *via* the synthetic route illustrated in Scheme 1. The reaction precursors of 1-phenyl-2-(4-(4,4,5,5-tetramethyl-1,3,2-dioxaborolan-2-yl)phenyl)-1*H*-phenanthro[9,10-d]imidazole(PPIB), 4′-bromo-2-methyl-1,1′-biphenyl(BrP1M), 4-bromo-2,5-dimethyl-1,1′-biphenyl (BrP2M), and 4′-bromo-2,4,6-trimethyl-1,1′-biphenyl(BrP3M) were prepared according to the previous reports[35]. 4-bromo-2,3,5,6-tetramethyl-1,1′-biphenyl (BrP4M) was synthesized by the Suzuki coupling reaction. The target molecules PP1M, PP2M, PP3M and PP4M were obtained by Suzuki coupling reactions

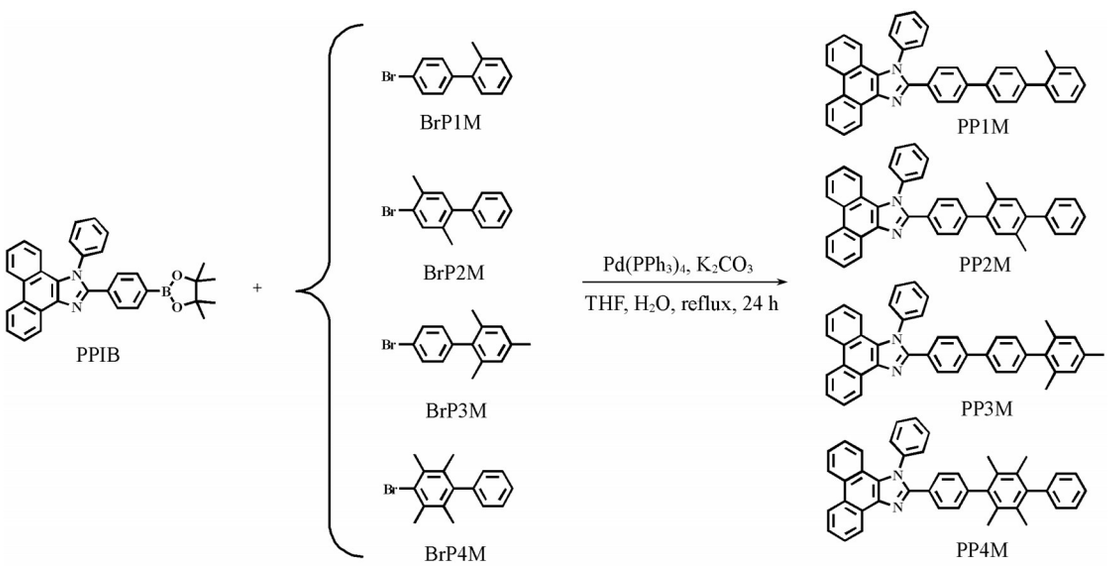

Scheme 1 Synthetic routes of PP1M, PP2M, PP3M, and PP4M

between PPIB and BrP1M, BrP2M, BrP3M and BrP4M with high yields from 64% to 83%, respectively. The final products were further purified by column chromatography and sublimation under vacuum. The chemical structure and purity of the resulting compounds were characterized by ^{1}H NMR (Fig.S1—S4 in the supporting information of this paper) and ^{13}C NMR, mass spectra, and corresponded well with their expected structures.

3 Results and Discussion

3.1 Thermal and Electrochemical Properties

The thermal stability of these compounds was evaluated using thermogravimetric analysis (TGA). As shown in Fig.1 and Table 1, the decomposition temperatures (T_ds, corresponding to 5% mass loss) of PP1M, PP2M, PP3M, and PP4M were examined as 411, 389, 413, and 408 ℃, respectively, indicating the good thermal stability of these compounds during the vacuum sublimation process. To access the morphological stability of these emitters at high operating temperature, the differential scanning calorimetry (DSC) measurements were also conducted. The DSC curves of PP1M and PP2M both displayed the glass transition temperature (T_g) at 112 ℃. In the DSC curves of PP3M and PP4M, the endothermic melting temperature (T_m) were observed at 327 and 301 ℃, suggesting that the T_m was reduced with the increasement of the number of methyl groups. In addition, T_g and crystallization temperature (T_c) were also observed in the DSC curve of PP4M, corresponding to 141 and 225 ℃, respectively. These thermal analyses indicate that all the four compounds exhibit sufficient thermal stability to withstand high-temperature vacuum evaporation.

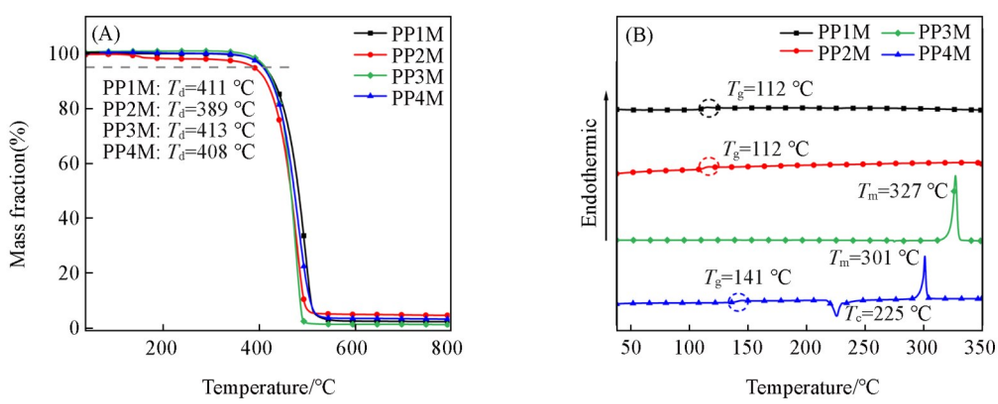

Fig. 1 TGA(A) and DSC(B) curves of PP1M, PP2M, PP3M, and PP4M*

Table 1 Key thermal and photophysical properties of PP1M, PP2M, PP3M, and PP4M*

Compound	T_d/T_g/T_c/T_m/℃	λ_{PL}/nm	FWHM	τ/ns	PLQY(%)	$10^{-8}k_r$/(s^{-1})	HOMO/LUMO(eV)
		Neat/doped	Neat/doped	Neat/doped	Neat/doped	Neat/doped	
PP1M	411/112/–/–	438/402	84/57	2.56/1.78	72.7/81.1	2.84/4.56	−5.50/−2.43
PP2M	389/112/–/–	400/395	66/41	2.25/1.96	58.4/60.6	2.60/3.14	−5.49/−2.53
PP3M	413/–/327/–	439/400	77/50	1.67/1.66	85.3/86.3	5.11/5.20	−5.48/−2.45
PP4M	408/141/225/301	401/393	68/38	2.21/1.93	20.7/9.0	0.94/0.74	−5.51/−2.63

* T_d: thermal decomposition temperature at a weight percentage of 95%; T_g: glass transition temperature; T_c: crystallization temperature; T_m: melting temperature; λ_{PL}: emission peak in neat films and 20%(mass fraction) doped films in CBP; FWHM: full width at half maxima in neat films and 20% doped films in CBP, τ: lifetime in neat films and 20% doped films; PLQY: photoluminescence quantum yields of neat films and 20% doped films; k_r: radiative transition rate constants of neat films and 20% doped films; HOMO/LUMO energy levels estimated by cyclic voltammetry measurement.

To quantitatively evaluate the influence of methyl substitution on the band gap of these materials, the onset oxidation and reduction potentials of four molecules were measured *via* cyclic voltammetry (CV) measurements. As shown in Fig.2, all the four compounds exhibited reversible oxidation processes, with onset

oxidation potentials (E_{ox}) similarly around 0.92 V for PP1M, PP2M, PP3M, and PP4M, indicating that the HOMOs of these four molecules were all determined by PPI units. The HOMO energy levels of PP1M, PP2M, PP3M, and PP4M were calculated to be −5.50, −5.49, −5.48, and −5.51 eV, respectively. In contrast, although these compounds all displayed irreversible reduction processes, the onset reduction potentials (E_{red}) exhibited a distinct alteration, which were −2.43, −2.53, −2.45, and −2.63 V for PP1M, PP2M, PP3M, and PP4M, respectively. This variation indicated that the number and location of methyl group substitution showed an influence on their electron cloud distribution of the LUMO energy level. The LUMO energy levels were estimated to be −2.29, −2.19, −2.27, and −2.09 eV, respectively. It could be observed that introduction of methyl groups between PPI and biphenyl segments significantly elevated the LUMO energy level. As a result, the LUMO levels showed the trend of PP4M>PP2M and PP3M>PP1M, which indicated that increasing the number of methyl groups also raised the LUMO levels.

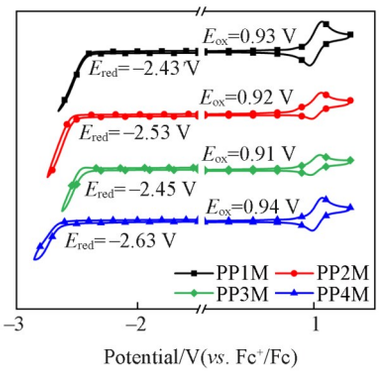

Fig. 2 Cyclic voltammetry curves of PP1M, PP2M, PP3M, and PP4M

3.2 Theoretical Calculations

To validate the proposed molecular design strategy and assess the effect of methyl group at different positions on the excited state properties, the theoretical calculations were performed using Gaussian program for density functional theory (DFT) calculation based on B3LYP/6-31g(*d*,*p*). The optimized geometries of ground state (S_0) and distribution of FMOs were displayed in Fig.3. All the four molecules showed a similar big torsion angel (75.12°—79.44°) between PPI and the benzene at the N1 site, and small torsion angel (24.78°—28.12°) between PPI and benzene at C1 position. In particular, the two peripheral benzene segments in PP3M and PP4M both exhibited orthogonal spatial configurations with torsion angles of 89.59° and 88.31°, indicating that the introduction of more methyl groups gave rise to bigger spatial hindrance and larger dihedral angles. The increasement of the dihedral angles between the benzene rings effectively suppressed π-conjugation, making it more difficult for the delocalization of π electrons along the molecule, resulting in nearly interrupted conjugations.

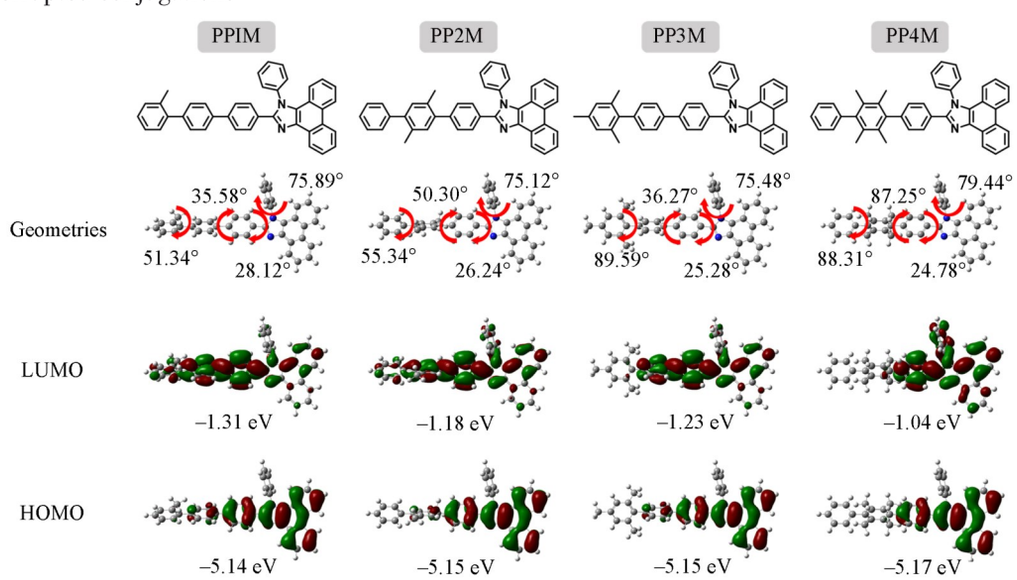

Fig. 3 Optimized geometries and FMOs of PP1M, PP2M, PP3M, and PP4M

The HOMO distribution of the four molecules was basically the same, which was mainly located on the electron-donating PPI unit, and the HOMO orbitals of PP1M, PP2M, and PP3M all showed little extension to the benzene ring directly connecting with PPI. The HOMO energy levels of the four emitters were all calculated to be around −5.15 eV. The LUMO energy levels and distribution of these four molecules showed obviously difference. The LUMO of PP1M and PP2M exhibited a sizable distribution on the terminal biphenyl ring on account of the moderate torsion angles, while the LUMO of PP3M displayed prominent distribution on the imidazole part in PPI and central benzene rings, and there was almost no distribution on the terminal biphenyl unit for the LUMO of PP4M. As a result, the computed LUMO energy levels of PP1M, PP2M, PP3M, and PP4M were −1.31, −1.18, −1.23, and −1.04 eV, respectively. The sequence of the calculated values of LUMOs were consistent well with the electrochemical results obtained from cyclic voltammetry.

The time-dependent DFT(TD-DFT) calculation and natural transition orbital(NTO) analyses for the four compounds were carried out to get a deeper understanding of their excited states. As shown in Fig.S5—S9(see the supporting information of this paper), their NTOs of S_1 and T_3 all displayed typical HLCT-type distributions. The NTO of $S_1 \rightarrow S_0$ for PP1M and PP3M owned high oscillator strengths(f>1.5000). However, due to less NTO overlap of $S_1 \rightarrow S_0$ of PP2M, the value of f was decreased to 1.3925. The least NTO overlap of PP4M resulted in the f of only 0.6338. These results suggested that excessive inhibition of conjugation might significantly restrain the radiative transition process of the emitters. As shown in Fig.S10(see the supporting information of this paper), the energy gaps between T_3 and S_1 were all approximately 0.10 eV for the four molecules, suggesting the potential hot exciton channels *via* the $T_3 \rightarrow S_1$ hRISC pathway.

3.3 Photophysical Properties

To investigate the photophysical properties, the UV-Vis absorption and PL spectra were measured in solvent with different polarity. As shown in Fig.S11(see the supporting information of this paper), the absorption spectral profiles and peak positions of all emitters in dilute solution(10^{-5} mol/L) remained largely unchanged with increasing solvent polarity, indicating the weak CT properties in the ground state. The strong absorption around 330 nm was attributed to the transition from the ground state to the lowest excited state, while the relatively weaker absorption near 360 nm corresponded to the π-π^* transition of the PPI unit. As illustrated in Fig.4, the PL spectra of all the four compounds in low-polarity solvents displayed vibrational fine structure and near-ultraviolet(NUV) emission, which was consistent with weak intramolecular CT state. With the increasement of solvent polarity, the vibrational structures of PL spectra for PP1M, PP2M, and PP3M gradually disappeared, accompanied by the red-shifts of 14, 21, and 34 nm, respectively. In contrast, PP4M retained its vibrational feature even in acetonitrile with the highest polarity, with only a minor red-shift of 4 nm, indicating that the S_1 state of PP4M was dominated by LE state. Detailed solvation photophysical data for PP1M, PP2M, PP3M, and PP4M were summarized in Table S1—S4(see the supporting information of this paper). Furthermore, the Lippert-Mataga model on the basis of the data of Stokes shift was plotted to evaluate the properties of excited states. As shown in Fig.S12(see the supporting information of this paper), PP1M, PP2M, PP3M, and PP4M all showed linear correlation between Stokes shift and solvent polarity with dipole moments of 7.7, 10.6, 13.2, and 5.1 D, which demonstrated the HLCT characteristic of all emitters and stronger CT characteristics of PP2M and PP3M as compared to PP1M and PP4M. The linear correlation between Stokes shift and solvent polarity indicated that the attributes of S_1 state were kept almost unchanged in either low polar solvents or high polar ones. Therefore, the S_1 states of them consist of HLCT states. PP4M exhibited a higher ratio of LE component as compared to PP1M, P2MP, and PP3M(Fig.S13, see the supporting information of this paper)[39].

In order to determine the S_1 and T_1 energy levels and the singlet-triplet energy splitting(ΔE_{ST}) of the four

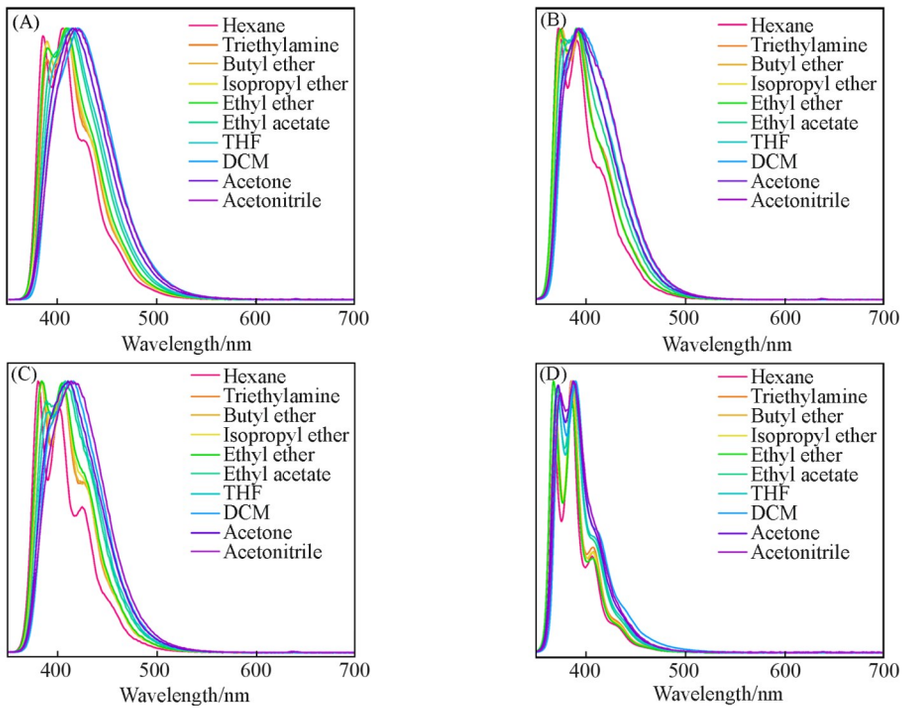

Fig. 4 PL spectra of PP1M(A), PP2M(B), PP3M(C), and PP4M(D) in different solvents

compounds, the low temperature fluorescence and phosphorescence spectra were measured in the glass state THF matrix at 77 K (Fig. S14, see the supporting information of this paper). The S_1 energy levels were examined to be 2.99, 3.13, 3.10, and 3.26 eV for PP1M, PP2M, PP3M, and PP4M, and the T_1 energy levels were determined as 2.33, 2.48, 2.54, and 2.53 eV, respectively. As a result, the ΔE_{ST} values of PP1M, PP2M, PP3M, and PP4M were calculated to be 0.66, 0.65, 0.56, and 0.67 eV, respectively. Such large ΔE_{ST} values indicated that the RISC process from T_1 to S_1 was unlikely to happen among these molecules, excluding the TADF channel of harvesting triplet exciton.

As shown in Fig.5, the PL spectra of these four compounds in neat films and doped films with doping concentration of 20%(mass fraction) in host(CBP) were measured. All the doped films showed the NUV emission peaks at around 400 nm. Notably, the doped films of PP2M and PP4M exhibited relatively narrow FWHMs of 41 nm and 38 nm, respectively, which can be primarily attributed to the effective suppression of molecular vibrations by methyl substitution. In contrast, the doped films of PP1M and PP3M showed somewhat broader FWHMs of 54 nm and 50 nm, consistent with their stronger intramolecular charge-transfer character. All the materials displayed small FWHMs, indicating their potential for achieving highly saturated deep-blue and near-ultraviolet electroluminescence[40,41]. The neat films of all the compounds showed similar trends but exhibited broader emission profiles compared to their doped counterparts, which is ascribed to aggregation effects. The red-shifts from doped to neat films were more pronounced for PP1M(36 nm) and PP3M(39 nm) than for PP2M(5 nm) and PP4M(8 nm), suggesting stronger CT properties of PP1M and PP3M. The absolute PLQYs of neat films based on PP1M, PP2M, PP3M, and PP4M were measured to be 72.7%, 58.4%, 85.3%, and 20.7%. The PLQY trend(PP3M>PP1M>PP2M>PP4M) aligned well with the f values predicted theoretically. We further characterized the PL decays of these films, and all the films exhibited PL lifetimes of approximately 2 ns. Among them, PP3M-based films exhibited the highest radiative rate constants (k_r) of 5.11×10^8 s^{-1}(neat) and 5.20×10^8 s^{-1}(doped), about one order of magnitude greater than their non-radiative rates(k_{nr}), which was beneficial for achieving high efficiency NUV emission. The radiation transition process of PP4M in solid state was not competitive compared with the non-radiation transition process, which might limit the EL performance.

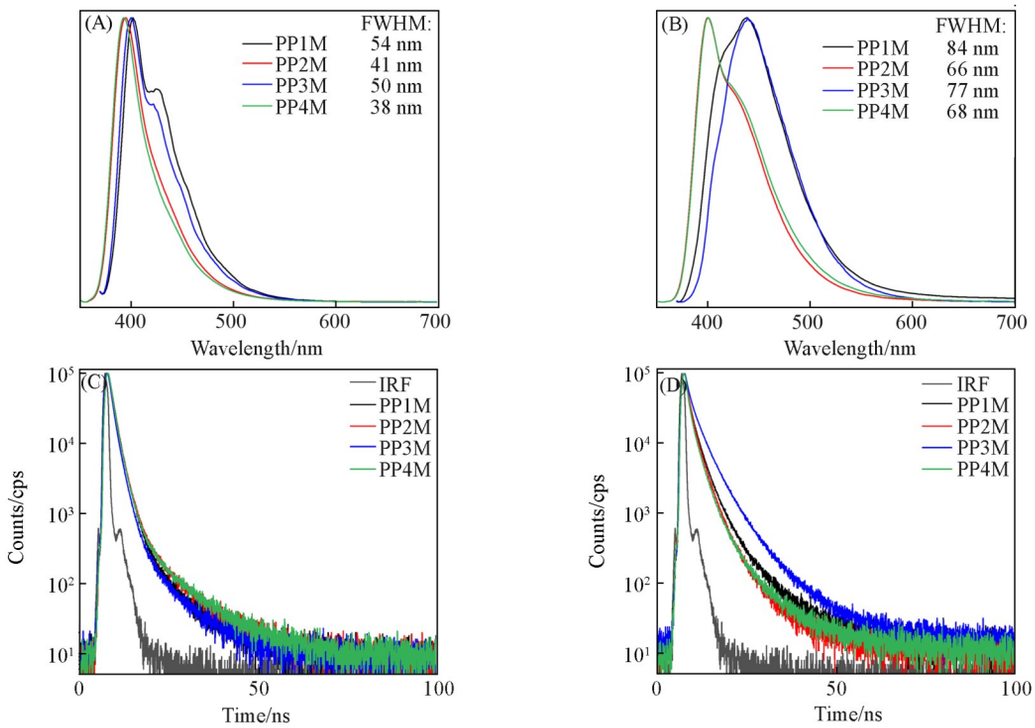

Fig. 5 PL spectra of 20% doped(A) and non-doped(B) films based on PP1M, PP2M, PP3M, and PP4M and PL decays of 20% doped(C) and non-doped(D) films in CBP based on PP1M, PP2M, PP3M, and PP4M

3.4 Electroluminescence Properties

To evaluate the potential of these materials for deep-blue OLED applications, the non-doped devices employing PP1M, PP2M and PP3M as the emitting layer were fabricated *via* vacuum evaporation. The device structure was optimized as ITO/HAT-CN (6 nm)/TAPC (25 nm)/TCTA (15 nm)/emitters (20 nm)/TmPyPB (40 nm)/LiF (1 nm)/Al (100 nm), in which Al and indium tin oxide (ITO) were applied as cathode and anode, LiF and 1,4,5,8,9,11-hexaazatriphenylene-hexanitrile (HAT-CN) served as the electron injection layer and the hole injecting layer, respectively, 3,3′-[5′-[3-(3-pyridinyl)phenyl][1,1′:3′,1″-terphenyl]-3,3″-diyl]bispyridine (TmPyPB) was selected as the electron transporting layer and di-(4-(*N*,*N*-ditolyl-amino)-phenyl)cyclohexan (TAPC) was the hole transporting layer, tris(4-carbazoyl-9-ylphenyl)amine (TCTA) was used as the exciton blocking layer. The electroluminescence spectra of the non-doped devices were shown in Fig.6 (A) and (B) (insets) and the EL data were summarized in Table 2. The EL peaks (Fig.S15, see the supporting information of this paper) of the PP1M, PP2M, and PP3M-based non-doped devices were located at 436, 416, and 432 nm, with the CIE coordinates of (0.15, 0.10), (0.16, 0.06), and (0.16, 0.08), respectively [Fig.6(C)]. The corresponding FWHM values were 78, 57 and 62 nm, respectively, which was consistent with the photophysical characteristics of their non-doped films. In contrast, PP1M and PP3M-based non-doped devices achieved the relatively high maximum EQEs of 7.6%, whereas the PP2M-based device reached only 4.0%. Furthermore, the PP3M-based non-doped device retained an EQE of 5.9% at the luminance of 1000 cd/m^2, and achieved a maximum luminance (L_{max}) of exceeding 10000 cd/m^2 [Fig.6(A) and (B)]. As a result, the PP3M-based non-doped device realized the high-efficiency deep-blue emission that met the NTSC standard.

We further fabricated doped OLEDs (20%, mass fraction) using CBP as a host material. As displayed in Fig. 6, the doped devices all exhibited blue-shifted and narrower emission spectra compared with their non-doped devices. The EL peaks (Fig.S16, see the supporting information of this paper) of PP1M, PP2M, and PP3M-based doped devices were located 428, 412 and 420 nm, with corresponding FWHM values of 66,

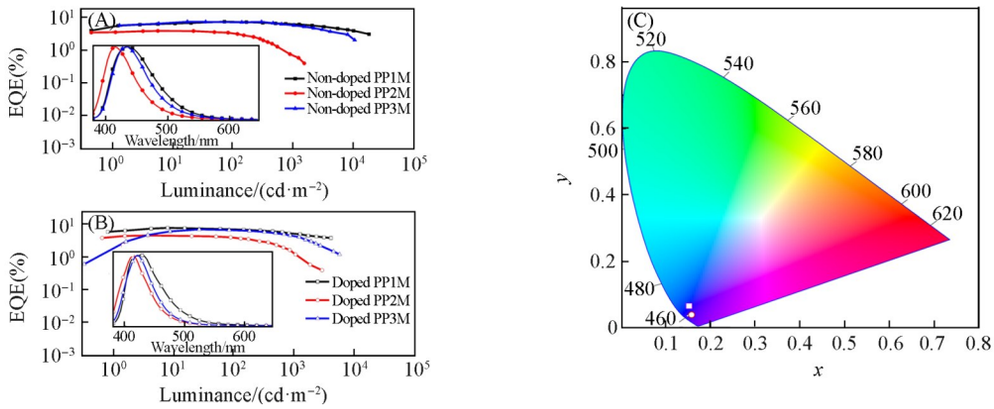

Fig. 6 EQE *versus* luminance curves and normalized EL spectra(insets) of non-doped devices(A) and doped devices(B), and CIE coordinates of doped devices(C)

Table 2 EL performances of non-doped and doped devices based on PP1M, PP2M and PP3M*

Emissive layer	V_{on}/V	L_{max}/(cd·m^{-2})	CE_{max}/(cd·A^{-1})	PE_{max}/(lm·W^{-1})	EQE(%)	λ_{EL}/nm	CIE/(x, y)	FWHM/nm
PP1M	3.1	18638	6.31	5.67	7.6/6.4	436	(0.15, 0.10)	78
PP2M	3.3	1564	1.63	1.47	4.0/0.8	416	(0.16, 0.06)	57
PP3M	3.0	10777	5.59	5.49	7.6/5.9	432	(0.16, 0.08)	62
20%PP1M:CBP	3.3	4343	4.71	4.23	8.0/5.3	428	(0.16, 0.07)	66
20%PP2M:CBP	3.3	3090	1.32	1.18	4.7/1.4	412	(0.16, 0.04)	52
20%PP3M:CBP	3.1	6030	2.85	2.42	7.2/4.7	420	(0.16, 0.04)	53

* V_{on}: turn-on voltage; L_{max}: maximum luminance; CE_{max}: maximum current efficiency; PE_{max}: maximum power efficiency; EQE: external quantum efficiency of the maximum at 1000 cd/m^{-2}; λ_{EL}: EL emission peak; FWHM: full width at half maximum.

52, and 53 nm, respectively. The CIE coordinates were determined to be (0.16, 0.07), (0.16, 0.04), and (0.16, 0.04), respectively. The PP2M-based and PP3M-based doped devices meet the BT.2020 standard of (0.131, 0.046). In addition, the PP3M-based doped device showed a low V_{on} of 3.1 V and attained a maximum EQE of 7.2%, maintaining 4.7% at the luminance of 1000 cd/m^2. It was worth noteworthy that the device achieved a L_{max} exceeding 6000 cd/m^2(Fig.S17, see the supporting information of this paper), which was the leading level in saturated deep-blue OLEDs that meets BT.2020 standard. Besides, the PP1M-based doped device also realized a high EQE of 8.0%. The linear relationship of current density-luminance(*J-L*) demonstrated that triplet-triplet annihilation(TTA) mechanism was not dominant for the enhancement of exciton utilization(Fig.S18, see the supporting information of this paper). The TADF mechanism could also be reasonably excluded based on the large values of ΔE_{ST} and the absence of delayed component in the PL decay profiles. Considering the potential hRISC channel presented by theoretical calculation, the hot exciton mechanism should be the main pathway for triplet exciton harvesting in these devices. The comparative analysis with recently reported deep-blue HLCT emitters($CIE_y \leqslant 0.06$) is provided in Table S5 and Fig.S19(see the supporting information of this paper) to benchmark the performance of PP1M, PP2M and PP3M.

4 Conclusions

In summary, four deep-blue hot exciton emitters, PP1M, PP2M, PP3M, and PP4M are designed and synthesized by incorporating methyl-substituted biphenyl units onto the PPI chromophore. Theoretical and experimental analyses reveal that methyl introduction, particularly with increasing substitution number, effectively restricts π-conjugation and enlarges the band gap of the resulting molecules. Notably, PP3M-based doped film achieves the highest PLQY of 85.3% and k_r of 5.20×10^8 s^{-1} in neat film. PP3M-based doped device realizes the best EL performance among these emitters, with a maximum EQE of 7.2%, a maximum luminance exceeding 6000 cd/m^2, a narrow FWHM of 53 nm and CIE coordinates of (0.16, 0.04), which

meets well with the BT. 2020 standard. These results provide a reliable molecular design strategy for the development of high-performance deep-blue hot exciton emitters.

The supporting information of this paper see http://www.cjcu.jlu.edu.cn/CN/10.7503/cjcu20250403.

References

[1] Tang C. W., VanSlyke S. A., *Appl. Phys. Lett.*, **1987**, *51*(12), 913—915
[2] Baldo M., Thompson M. E., Forrest S., *Nature.*, **2000**, *403*(6771), 750—753
[3] Zhen C. G., Chen Z. K., Liu Q. D., Dai Y. F., Shin R. Y. C., Chang S. Y., Kieffer J., *Adv. Mater.*, **2009**, *21*(23), 2425—2429
[4] Jiang Z., Liu Z., Yang C., Zhong C., Qin J., Yu G., Liu Y., *Adv. Funct. Mater.*, **2009**, *19*(24), 3987—3995
[5] Sun Z., Yin P., He S., Zhang K., Pan X., Wang J., Hao P., Zhou Z., Yang X., Ma L., Tan C., *Chem. Res. Chin. Univ.*, **2025**, *41*(3), 519—524
[6] Lee H., Lee J., Lee J. I., Cho N. S., *Elec.*, **2018**, *7*(9), 155
[7] Ochi J., Yamasaki Y., Oda S., Kondo M., Ikeno A., Kondo Y., Hatakeyama T., *Adv. Opt. Mater.*, **2025**, *13*(23), 2402939
[8] Michalis M., *Eur. J. Commun.*, **1999**, *14*(2), 147—171
[9] Lim H., Woo S. J., Ha Y. H., Kim Y. H., Kim J. J., *Adv. Mater.*, **2022**, *34*(1), 2100161
[10] Du C., Liu H., Cheng Z., Zhang S., Qu Z., Yang D., Qiao X., Zhao Z., Lu P., *Adv. Funct. Mater.*, **2023**, *33*, 2304854
[11] Wang Z. M., Feng Y., Li H., Song X. H., Lu P., *Chem. J. Chinese Universities.*, **2014**, *35*(8), 1691—1696(王志明, 冯颖, 李辉, 宋晓慧, 路萍. 高等学校化学学报, **2014**, *35*(8), 1691—1696)
[12] Chen P., Zhang G., Li J., Ma L., Zhou J., Zhu M., Li S., Wang Z., *Chem. Res. Chin. Univ.*, **2024**, *40*(2), 293—304
[13] Sugawara M., Choi S. Y., Wood D., *IEEE. Signal. Proc. Mag.*, **2014**, *31*(3), 170—174
[14] Yang J., Lou J., Ni M.; Zhuo Z., Li H., An X., Sun N., Li M., Wang Z., Huang W., *Chem. Eng. J.*, **2025**, *524*(15), 168961
[15] Wu G., Ge X., Yang Z., Liu Y., Chen Z., Wang Y., Li G., Guo D., Deng H., Zhao J., Chi Z., *Chem. Eng. J.*, **2024**, *497*, 154
[16] Shang A., Zhao L., Li Z., Cheng Z., Jin H., Feng Z., Chen Z., Zhang H., Lu P., *Chem. Res. Chin. Univ.*, **2022**, *38*(6), 1461—1466
[17] Feng C., Zhang K., Zhang B., Feng L., He L., Chen C. F., Li M., *Angew. Chem. Int. Ed.*, **2025**, *64*(10), e202425094
[18] Xiong J., Wu M., Yao L. Y., *Chem. Res. Chin. Univ.*, **2024**, *40*(5), 887—893
[19] Shahalizad A., Malinge A., Hu L., Laflamme G., Haeberlé L., Myers D. M., Mao J., Skene W. G., Kéna-Cohen S., *Adv. Funct. Mater.*, **2021**, *31*(1), 2007119
[20] Xu J., Wang M., Chen J., Wu Z., Guo T., Tang B. Z., Zhao Z., *Adv. Opt. Mater.*, **2024**, *12*(23), 2400739
[21] Kim H. M., Choi J. M., Lee J. Y., *RSC. Adv.*, **2016**, *6*(6815), 64133
[22] Feng Z., Cheng Z., Su Z., Wan L., Ge S., Liu H., Ma X., Liu F., Lu P., *Adv. Opt. Mater.*, **2024**, *12*, 2302839
[23] Xie F., Yang X., Jin P., Wang X. T., Ran H., Zhang H., Sun H., Su S. J., Hu J. Y., *Adv. Opt. Mater.*, **2023**, *11*(4), 2202490
[24] Noda H., Chen X. K., Nakanotani H., Hosokai T., Miyajima M., Notsuka N., Kashima Y., Brédas J. L., Adachi C., *Nat. Mater.*, **2019**, *18*(10), 1084—1090
[25] Gao S., Chen X., Ge X., Chen Z., Zhao J., Chi Z., *Chem. Res. Chin. Univ.*, **2022**, *38*(6), 1526—1531
[26] Tsuchiya Y., Mizukoshi K., Saigo M., Ryu T., Kusuhara K., Miyata K., Onda K., Adachi C., *Nat. Commun.*, **2025**, *16*(1), 4815
[27] Wang Z., Hu X., Yan Z., Liang J., Song X., Chen Q., Bi H., Wang Y., *Adv. Sci.*, **2025**, *12*(9), 2410479
[28] Hatakeyama T., Shiren K., Nakajima K., Nomura S., Nakatsuka S., Kinoshita K., Ni J., Ono Y., Ikuta T., *Adv. Mater.*, **2016**, *28*(14), 2777—2781
[29] Mamada M., Aoyama A., Uchida R., Ochi J., Oda S., Kondo Y., Kondo M., Hatakeyama T., *Adv. Mater.*, **2024**, *36*(30), 2402905
[30] Ochi J., Yamasaki Y., Tanaka K., Kondo Y., Isayama K., Oda S., Kondo M., Hatakeyama T., *Adv. Optical Mater.*, **2025**, *13*(14), e70128
[31] Ochi J., Yamasaki Y., Oda S., Kondo M., Ikeno A., Kondo Y., Hatakeyama T., *Adv. Optical Mater.*, **2025**, *13*(23), e70128.
[32] Li W., Liu D., Shen F., Ma D., Wang Z., Feng T., Xu Y., Yang B., Ma Y., *Adv. Funct. Mater.*, **2012**, *22*(13), 2797—2803
[33] Xu Y., Xu P., Hu D., Ma Y., *Chem. Soc. Rev.*, **2021**, *50*(2), 1030—1069
[34] Wang S., Qi H., Huang H., Li J., Liu Y., Xue S., Ying S., Shi C., Yan S., *Mater. Chem. Front.*, **2025**, *9*(1), 55—64
[35] Chen R., Li S., Huang H., Tong X., Liu Y., Ren Z., Ying S., Liu L., Yan S., *Chem. Sci.*, **2025**, *16*(35), 16304—16313
[36] Hu C. H., Sang Y., Yang Y. W., *Chem*, **2023**, *9*(10), 2997—3012
[37] Huh J. S., Ha Y. H., Kwon S. K., *ACS Appl. Mater. Interfaces*, **2020**, *12*(13), 15422—15429
[38] Obermann S., Zheng W., Melidonie J., *Chem. Sci.*, **2023**, *14*, 8607—8614
[39] Lu T., Chen F., *J. Comput. Chem.*, **2012**, *33*, 580—592
[40] Li J. Q., Huang F., Xie Y., *Aggregate*, **2025**, *6*(11), e70177
[41] Eisfeld A., Vlaming S. M., Malyshev V. A., Knoester J., *Phys. Rev. Lett.*, **2010**, *105*, 137402

(Ed.: H, K, M)